Novel Hollow Mesoporous 1D TiO_2 Nanofibers as Photovoltaic and Photocatalytic Materials

Xiang Zhang [a b], Velmurugan Thavasi [c], S G Mhaisalkar [b] and Seeram Ramakrishna * [a d]

Received (in XXX, XXX) Xth XXXXXXXXX 20XX, Accepted Xth XXXXXXXXX 20XX
DOI: 10.1039/b000000x

Hollow mesoporous one dimensional (1D) TiO_2 nanofibers are successfully prepared by co-axial electrospinning of titanium tetraisopropoxide (TTIP) solution with two immiscible polymers; polyethylene oxide (PEO) and polyvinylpyrrolidone (PVP) using core-shell spinneret, followed by annealing at 450°C. The annealed mesoporous TiO_2 nanofibers are found to be hollow structure with an average diameter of 130 nm. Measurements using Brunauer–Emmett–Teller (BET) method reveals that hollow mesoporous TiO_2 nanofibers possess high surface area of 118 m^2 /g with two types of mesopores; 3.2 nm and 5.4 nm that resulted from gaseous removal of PEO and PVP respectively during annealing. With hollow mesoporous TiO_2 nanofibers as photoelectrode in dye sensitized solar cells (DSSC), the solar-to-current conversion efficiency (η) and short circuit current (Jsc) are measured as 5.6 % and 10.38 mA/cm^2 respectively, which are higher than that of DSSC made using regular TiO_2 nanofibers under identical conditions (η = 4.2 %, Jsc = 8.99 mA/cm^2). The improvement on the conversion efficiency is mainly attributed to higher surface area and mesoporous TiO_2 nanostructure. It facilitates the adsorption of more dye molecules and also promotes the incident photon to electron conversion. Hollow mesoporous TiO_2 nanofibers with closely packing of grains and crystals intergrowth with each other demonstrates faster electron diffusion, and longer electron recombination time than that of regular TiO_2 nanofibers as well as P25 nanoparticles. The surface effect of hollow mesoporous TiO_2 nanofibers as photocatalyst on the degradation of rhodamine dye was also investigated. The kinetic study shows that the hollow mesoporous surface of the TiO_2 nanofibers influenced its interactions with the dye, and resulted in an increased catalytic activity over P25 TiO_2 nanocatalysts.

Introduction

Electrospinning has been popular in producing one dimensional (1D) metal oxides fibers or polymer fibers for energy based applications include as electrode in photovoltaic, fuel cells, energy storage devices and as photo catalysts. [1-3] High molecular weight polymers as structure directing agents, blended with metal oxide precursor and were drawn into composite fibers through a spinneret by applying a high voltage. Besides its application in energy, electronspun fibers could be also be used in other areas including wetting material, etc. Besenbacher et al produced the responsive biodegradable polycaprolactone nanofibers by functionalizing its surface with photoresposive azobenzene and shown a reversible light-driven wettability changes .[4]

Nanofibers may be preferred over nanoparticles in energy for the following reasons: faster electrons diffusion than in nanoparticles; fibers of diameter lesser than 150 nm provides an additional energetic barrier to recombination due to the formation of a space-charge region; 1D nanofibers ensure for the rapid collection of carriers generated by reducing surface.

A standard dye sensitized solar cell (DSSC) consists of TiO_2 nanoparticulate film as photoelectrode on transparent conducting oxide glass (fluorine doped tin oxide, FTO), a photosensitizer (dye), a platinum-coated FTO as counter electrode and an iodide/triiodide redox couple electrolyte.[5-8] Upon illumination, the sensitized dye injects electron into the conduction band of the TiO_2, which transports through the nanoparticulate matrix to FTO.[9] The electron-deficient dye is subsequently regenerated by the redox electrolyte. The performance of DSSCs was more closely related to the surface area of TiO_2 films.[10] More dye molecules could be anchored efficiently if the metal oxide is

[a] *Healthcare and Energy Materials Laboratory, Department of Mechanical Engineering, Singapore 117581, Singapore. Fax: +65-6773 0339; Tel:+65-6516 6593 E-mail: velnanotech@gmail.com; seeram@nus.edu.sg;*
[b] *Energy Research Institute, NTU, Singapore 639798, Singapore.*
[c] *NUS Nanoscience and Nanotechnology Initiative, Singapore 117581, Singapore.*
[d] *King Saud University, Riyadh 11451, Kingdom of Saudi Arabia*
† Electronic Supplementary Information (ESI) available: [details of any supplementary information available should be included here]. See DOI: 10.1039/b000000x/
‡ Footnotes should appear here. These might include comments relevant to but not central to the matter under discussion, limited experimental and spectral data, and crystallographic data.

provided with larger surface area, leading to stronger absorption of solar irradiation from the adsorbed dye.[11] There also has been a strong motivation to increase the active surface area of TiO_2 and also produce novel morphology because of its excellent catalytic activity. TiO_2 as photocatalyst has many advantages including UV absorption range, excellent chemical stability and relatively available in abundant.

Much research activities have been directed to develop the methodologies that produce metal oxide nanostructures with higher surface area as it facilitates for the adsorption of more dye molecules in photovoltaic and greater catalytic activity. Methods such as electrodeposition, hydrothermal, potentiostatic anodization, chemical and bio-based templates were employed to obtain higher surface area. Meng et al.[12] and Grimes et al.[13,14] prepared hollow hemispherical nano-TiO_2 and TiO_2 nanotube arrays respectively using radio frequency (RF) sputtering method.

There are few drawbacks associated with the synthesis of TiO_2 nanotube arrays directly on FTO for energy applications. For example, loose packing of TiO_2 nanotubes on FTO is common using synthetic method that results in recombination loss, reduces the conversion efficiency in solar cells. For the improvement of adhesion of TiO_2 nanotubes onto FTO, a thin layer of TiO_2 nanoparticulate film has been employed that however could render more free-contact space, increase ohmic loss and the dark current in solar cells.

Using electrospinning, well defined hollow structured materials were achieved either by using polymer as additive or volatile solvents or soluble oils as additives, or process temperature.[15] Xia et al.[16] demonstrated the formation of hollow TiO_2 nanowires using polystyrene (PS) in the electrospinning blend. However, no data about the surface area and also no specific applications were reported by these authors. Another group led by Kim[17,18] produced fine TiO_2 nanorods with higher surface area of 138 m^2/g by electrospinning the blend with their lab-synthesized polymer PVAc (polyvinyl acetate, m.wt 10^6). Nanorods morphology is relatively inferior for energy applications because the number of contact points in between the rods is quite more, hence electron trap is expected to be considerably significant in nanorods.[19]

The formation of porous structure enhances the interfacial surface area that is beneficial for energy devices. For instance, larger interfacial area between TiO_2 and dye in solar cells leads to high visible-light absorbance from the numerous successive monolayers of adsorbed dye, and also improves the accessibility of electrolyte to electrode.

Lofton et al.[20] produced porous TiO_2 fibers by electrospinning the sol gel precursor with sodium chloride/calcium carbonate, and subsequent removal of salt through leaching. This approach however also led to the formation of micro-size pores, which are undesirable for the application in solar cells. The electrons transport would be affected within the porous structure of TiO_2, in turn causes electron-hole recombination. The higher surface area of the porous TiO_2 film with the smaller pore size (< 5 nm) is critical for efficient device performance.

Considering the advantages of higher surface area and larger interfacial area by hollow and mesoporus structures respectively, an electrospinning method that is capable of generating both hollow and mesoporous structures within each fiber using cost-effective polymers has been developed. TiO_2 fiberous mat that possesses both hollow and mesoporous structures in each fiber was produced using co-axial electrospinning of precursors with polyethylene oxide (PEO) in the core, and polyvinylpyrrolidone (PVP) solution alone in shell part of the spinneret, followed by annealing to 450°C at ramp rate of 2°C/min. DSSCs were constructed using the as-prepared hollow mesoporous TiO_2 nanofibers as photoelectrode, and their performances were evaluated in comparison to regular and smooth TiO_2 nanofibers. It was found that DSSCs based on hollow mesoporous TiO_2 nanofibers exhibited a significant increase of 33 % in solar-to-current conversion efficiency over regular TiO_2 fibers.

As-obtained hollow mesoporous TiO_2 nanofibers mat was also investigated for its catalytic performance against the degradation of organic dye (rhodamine B) and compared with the P25 TiO_2 nanoparticles (NPs). The study revealed that the higher surface area resulted out of hollow mesoporous structure appears to be a promising morphology for TiO_2 to be as more effective photocatalyst.

Experimental

a. Materials

Titanium tetraisopropoxide [$Ti(O^iPr)_4$; 97%], solvents N,N-dimethylformamide (DMF, 99.8 %), ethanol (100 %) and acetic acid (99.7 %) were purchased from Sigma-Aldrich (Singapore). All chemicals were used as received without further purification. Cis-di(thiocyanato)-bis(2,20-bipyridyl-4-carboxylate-40-carboxylic acid)-ruthenium(II) (N719) dye was purchased from

Solaronix and used as sensitizer to harvest the solar radiation. All chemicals were used as received without further purification.

b. Core-shell electrospinning

Core-shell spinneret (Scheme 1) was set up with two needles of size of 27G (core) and 21G (shell) fixed coaxially. Two precursor gels were chosen such that they were immiscible in nature, one for the core liquid and another for the shell liquid.

For this study, the precursor solution for the shell side was prepared by dissolving 0.9 g of polyvinyl pyrrolidone (PVP, M_W= 100 000, Aldrich) in 10 ml of ethanol followed by the addition of 3 ml acetic acid. Titanium tetraisopropoxide (1.5 g) was then added into PVP solution under vigorous stirring for 12h. The precursor for core fluid was prepared by dissolving 0.5 g of polyethylene oxide (PEO, M_w = 900 000, Sigma-Aldrich) in 5 ml of DMF under heating at 50°C. As-prepared two precursor gels were loaded into two plastic syringes (5 ml) and connected to a coaxial core-shell spinneret (Scheme 1). A high-voltage power was applied to the needle tip. The flow rate for core and shell fluids was set to 0.2 ml/h and 0.6 ml/h respectively. The electric field strength was 15 kV and an aluminum foil wrapped plate collector was placed at 12 cm below the needle tip for the collection of fibers.

A compound (core and shell) droplet formed at the edge of spinneret nozzles and transformed into a Taylor cone [21] with a compound jet co-electrospun from its tip. The core-shell electrospun fibers were produced as in the simple electrospinning, the jet was pulled by the electric field, and stretched by the bending instability. The solvents from core and shell solution were evaporated rapidly due to set-humidity of 50% and concentrated core and shell solutions in the traveling path. The compound Taylor cone was subsequently formed with a shell droplet surrounded core solution droplet at the core-shell spinneret tip. PEO and PVP-TiO_2 were obtained as core and shell nanofibers respectively (Scheme 1). The electrospun core-shell nanofibers were calcined at 450°C for 1 h at a heating rate of 2°C/min to remove polymers, obtained hollow mesoporous nanofibers.

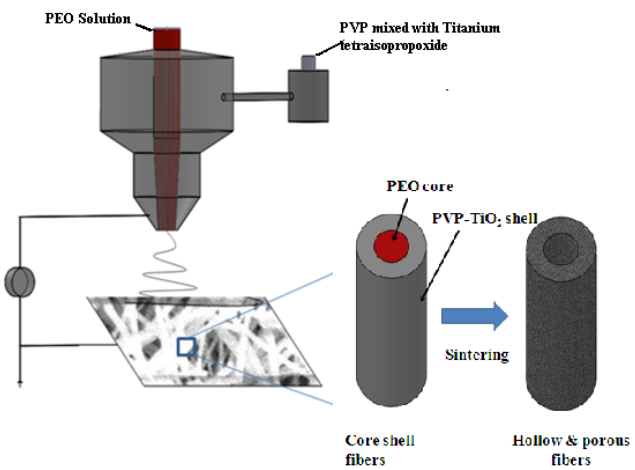

Scheme 1. Set up for co-electrospinning and core-shell nanofibers and removal of organic polymers from core and shell layers

For performance comparison with regular TiO_2 nanofibers, the precursor gel consisting of titanium (IV) isopropoxide (1.5 g), 0.9 g polyvinyl pyrrolidone (PVP, M_W= 100 000, Aldrich), 10 ml ethanol and 3 ml acetic acid was loaded into a plastic syringe and a 15 kV DC voltage was applied to the single nozzle spinneret. The flow rate was set to 1 ml/h. The collector was grounded and placed at a distance of 10 cm below the spinneret.

c. Characterizations

The morphology of the samples was examined by field emission scanning electron microscope (SEM, JEOL-6701F, Japan) operated at voltage of 10kV after platinum coating (20 mA/30s). The energy dispersive X-ray spectroscopy (EDS) is attached with the SEM machine. The average diameter of the TiO_2 nanofibers was measured using the software. Further examination on the calcined TiO_2 nanofibers were done using transmission electron microscopy (TEM, JEOL 3010, Japan) and selected area electron diffraction (SAED) operated at 200 kV. The samples were prepared by ultrasonic bath to disperse the TiO_2 nanofibers in ethanol followed by dropping the suspension on a carbon-coating copper grid. X-ray diffraction (XRD) was measured with Cu-Kα X-ray radiation at λ=1.54056Å with diffract grams recorded for 2θ between 10^o and 70^o. The surface area and pore volume were determined by nitrogen adsorption/desorption using Brunauer-Emmett-Teller (BET, Micromeretics Tristar 2000, surface area and pore size analyzer). The samples were degassed under inert nitrogen (N_2) at 300°C for 12 h prior to BET measurements (under standard protocols at 77 K). UV-Vis spectra were measured using Shimadzu UV-3600 UV-Vis-NIR spectrophotometer with a spectral resolution of 1 nm.

d. Photoelectric measurements

The fluorine-doped tin oxide (FTO) substrates were ultrasonically cleaned with DI water, acetone, and α-propanol. The paste was

made by adding 3.75 g hollow mesoporous nanofibers and 18.7 g ethyl cellulose (Aldrich) into 15.2 g α-terpineol (Aldrich). The paste was then sonicated for 2 h until a homogenous suspension without aggregate was obtained. After that, the TiO_2 paste was bladed on a FTO glass to a thickness of 12 ± 2 μm using a doctor-blading technique. The TiO_2 electrode was dried in air at 90°C for 30 min and calcined at 450°C for 1 h to completely remove ethyl cellulose and α-terpineol. Anchoring of the dye molecules on the hollow mesoporous TiO_2 nanofibers electrode surface was done by soaking the electrode in a 1:1 volume mixture of acetonitrile and tert-butanol of N719 dye (0.5 mM) for 24 h at room temperature. The TiO_2 photoelectrode was then washed with DI water to remove unanchored dye molecules and dried in desiccator. A 50 μm space was covered the TiO_2 electrode. A DSSC was assembled by sandwiching TiO_2 photo anode, counter electrode and filling with electrolyte solution which containing 0.1 M lithium iodide, 0.03 M iodine, 0.5 M 4-tert-butylpyridine, 0.6 M 1-propyl-2,3-imethylimidazoliumiodide (acetonitrile as solvent).

The performance of DSSC was obtained by photocurrent measurements of the assembled DSSC under irradiation of a 100 $mWcm^{-2}$ xenon lamp (Thermo Oriel Xenon Lamp 150 W: Model 66902) with AM 1.5 G, 1 sun condition. I-V curve was obtained via a potentiosat (Autolab PGSTAT30, Eco Chemie B.V, and The Netherlands). The amount of chemisorbed dye was performed by measuring the concentration of dye which was desorbed into a equal volume (20 mL) of diluted NaOH solution (0.1M). The relative difference of absorbance is translated to the relative difference of dye loading of TiO_2 electrode. The Incident photo-to-current conversion efficiency (IPCE) was measured by using a monochromator and a 300 W Xenon lamp with a spectral resolution of 5 nm. Electrochemical impedance spectroscopy (EIS) measurements were performed using AutoLab PSTAT30 with a frequency range of 0.05 Hz - 30 kHz in the dark. The amplitude of ac signal was set to be 10 mV.

e. Photocatalytic measurements

Rhodamine B was chosen as model pollutant to evaluate the photocatalytic performance of the samples. 0.05 g of TiO_2 sample was added into a 50mL rhodamine B solution with the concentration of 20 mg/L in quartz photoreactor. The mixed solution was stirred for 30 min in dark to achieve adsorption-desorption equilibrium. Then the reaction solution was irradiated in visible light using 200 W lamp. A glass filter was used as cutoff for short-wavelength components of light. A water-cooling system was performed to maintain the reaction solution at room temperature. The mixture solution was centrifuged and filtered through 0.22-μm Millipore membrane filter to filter out catalyts. Then the concentration of rhodamine B was measured by a UV-vis spectrophotometer with an acceptable error of ± 3%. The absorbance peak of rhodamine B was at 552 nm.

Results and Discussion

a. Morphology Characterization

The morphology of the TiO_2 nanofibers obtained by coaxial electrospinning using PEO as core and PVP mixed with titanium tetraisopropoxide as shell material were investigated. As-spun core-shell (PEO/TiO_2-PVP) composite nanofibers were found to be continuous as shown in Fig 1 (a). The inset is the as-spun core-shell (PEO/TiO_2-PVP) composite nanofibers deposited on aluminum foil. The fibers diameter varied between approximately 40 nm and 190 nm. A high magnified SEM image the core-shell (PEO/TiO_2-PVP) composite nanofibers are shown in Fig 1 (b). The surface of the composite nanofibers is relatively smooth. Fig 1 (c) illustrates the TEM image of these composite nanofibers. There is a thin layer of TiO_2-PVP composite shell uniformly covering the entire length of the core nanofibers (PEO). However, the shell layer is slightly unsymmetrical.

Upon sintering at 450 ^{0}C in the air for 1 h, the core-shell (PEO/TiO_2-PVP) nanofibers were converted to hollow mesoporous TiO_2 nanofibers. Figure 1 (e) shows the SEM micrographs of hollow mesoporous TiO_2 nanofibers. The average diameter of synthesized hollow mesoporous TiO_2 nanofibers was measured to be 130 ± 80 nm. PEO which was used as the core material found to be decomposed and removed during sintering, yielding the hollow structure in the core. Meanwhile, the PVP phase present in the shell layer was also found to be decomposed during sintering and produced ceramic TiO_2 with uniform mesoporous in the shell structure. SEM figures 1 (f) and (g) confirmed the formation of hollow nanostructures in the core and also mesoporous surface in the shell. The wall thickness of hollow mesoporous TiO_2 nanofibers was measured to be 28 ± 18 nm with slightly asymmetrical. Cross-sectional view of elliptical tubular tip is illustrated in Fig 1(h). As shown in Fig 1 (d), only Ti and O peaks are seen in the EDX spectrum and the molar ratio of Ti to O is around 1:2, which well agrees with the

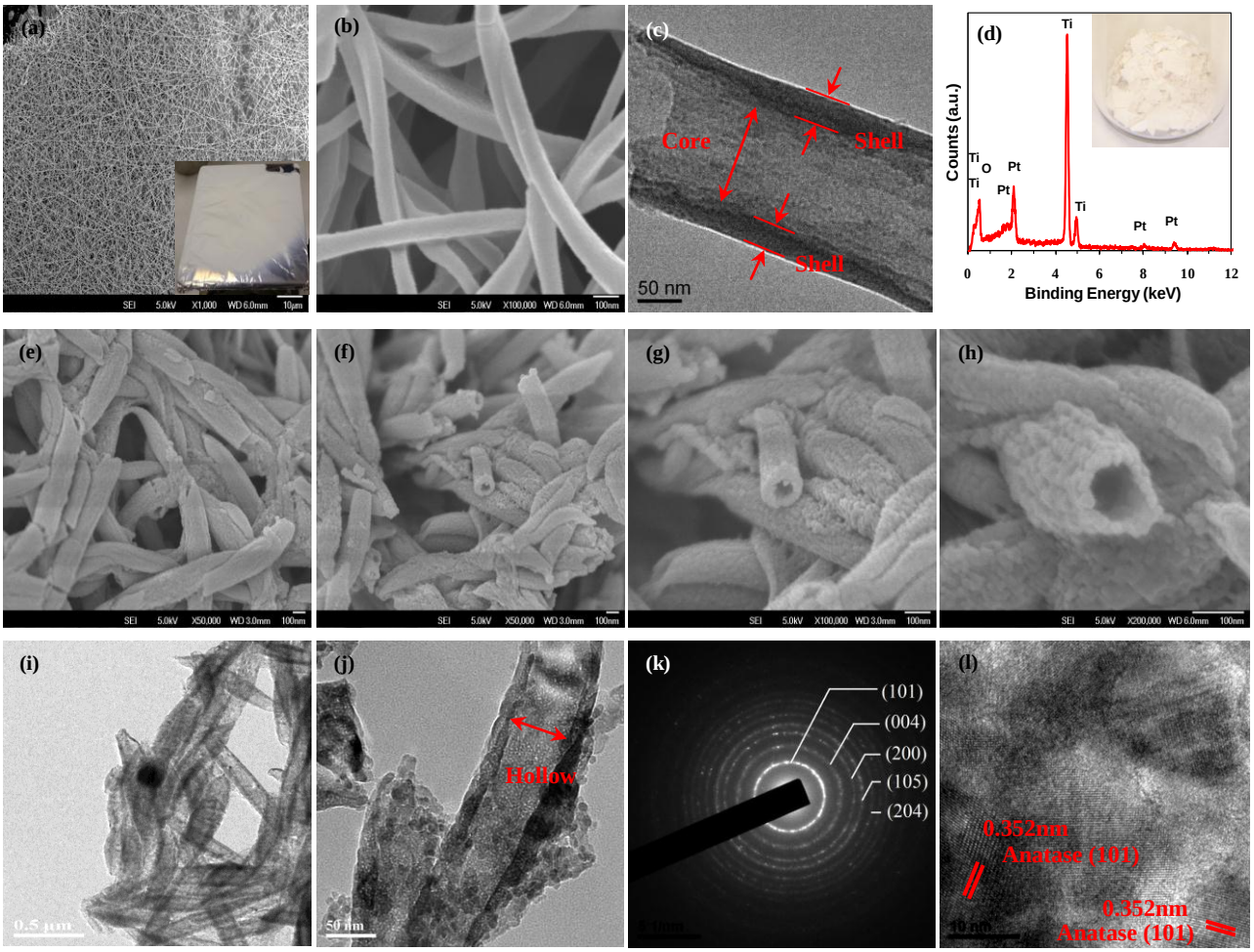

Fig 1. (a) SEM image of a bundle of core-shell (PEO/TiO_2-PVP) composite nanofibers.[The inset is the photo of core-shell (PEO/TiO_2-PVP) composite nanofibers samples] (b) Close-up image of a bundle of core-shell (PEO/TiO_2-PVP) composite nanofibers. (c) TEM image of core-shell (PEO/TiO_2-PVP) composite nanofibers. (d) EDX spectroscopy of hollow mesoporous TiO_2 nanofiber. [The inset is the photo of hollow mesoporous TiO_2 nanofibers samples] (e) SEM image of a bundle of hollow mesoporous TiO_2 nanofibers. (f) Tilted view image of a bundle of hollow mesoporous TiO_2 nanofibers. (g) Close-up tilted view image of a bundle of hollow mesoporous fibers TiO_2. (h) Close-up image of one single hollow mesoporous TiO_2 nanofibers. (i) TEM image of a bundle of hollow mesoporous TiO_2 nanofiber. (j) TEM image of one single hollow mesoporous TiO_2 nanofiber. (k) The corresponding SAED pattern. (l) HRTEM image of the anatase TiO_2 crystals indicated by red lines.

stoichiometric ratio of TiO_2. The inset is the optical image of hollow mesoporous TiO_2 nanofibers after sintering.

The microstructure of the hollow mesoporous TiO_2 fibers after sintering was further examined by transmission electron microscopy (TEM). Figure 1 shows typical microstructure of a bundle of hollow mesoporous TiO_2 nanofibers. A single hollow mesoporous TiO_2 nanofibers is illustrated in Fig 1 (j). The tubular shape and the pores on the surface of hollow mesoporous TiO_2 nanofibers were clearly observed. The corresponding crystalline diffraction rings of (101), (004), (200), (105) and (204) in the selected area electron diffraction (SAED) patterns (Fig 1 (k)) confirming that anatase phase of TiO_2 nanofibers was formed. It also demonstrates that the hollow mesoporous TiO_2 nanofibers were polycrystalline.

As shown in Fig 1 (l), high resolution TEM image revealed the hollow mesoporous TiO_2 nanofibers possessed well-crystallized structure and lattice fringes having interplanar spacing of 0.352 nm corresponding to TiO_2 anatase (101) plane.

The crystal structures of hollow mesoporous TiO_2 fibers were investigated by X-ray diffraction (XRD) (Figure 2). All diffraction peaks at 25.3° (101), 37.8° (004), 48.2° (200) and 54.1° (105) were assigned to pure anatase phase and no crystalline products. The peaks were rather sharp and in excellent agreement with the results from SAED analysis, indicating that the fibers were highly crystalline. There are no additional peaks

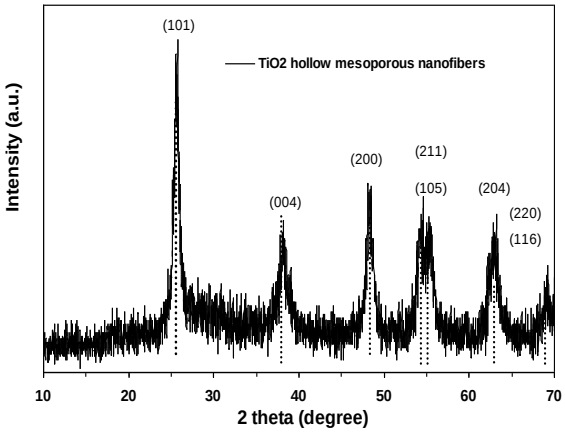

Fig 2. XRD pattern of hollow mesoporous TiO_2 nanofibers

observed in the XRD spectrum indicating no detective impurities. The average grain size of annealed hollow mesoporous TiO_2 nanofibers from the corresponding XRD peaks were determined by Scherrer equation [22]:

$$D = K \lambda / (\beta \cos\theta) \qquad (1)$$

where D is the crystallite size, K is shape factor and taken as 0.94 for a small cubic crystal of uniform size, λ is X-ray wavelength, β is full width at half the maximum intensity (FWHM) in radians and θ is the Bragg angle. The average crystallite size was calculated to be 9.6 nm.

The morphology of regular TiO_2 nanofibers was first investigated using SEM. Regular TiO_2 nanofiberous mat obtained after annealing at 450^{0}C in the air for 1 h were found to be continuous (Figure 3 (a)). The average diameter of synthesized regular TiO_2 nanofibers was measured to be 100 ± 63 nm. The highly crystallinity was observed on the surface of regular TiO_2 nanofibers (Figure 3 (b)).

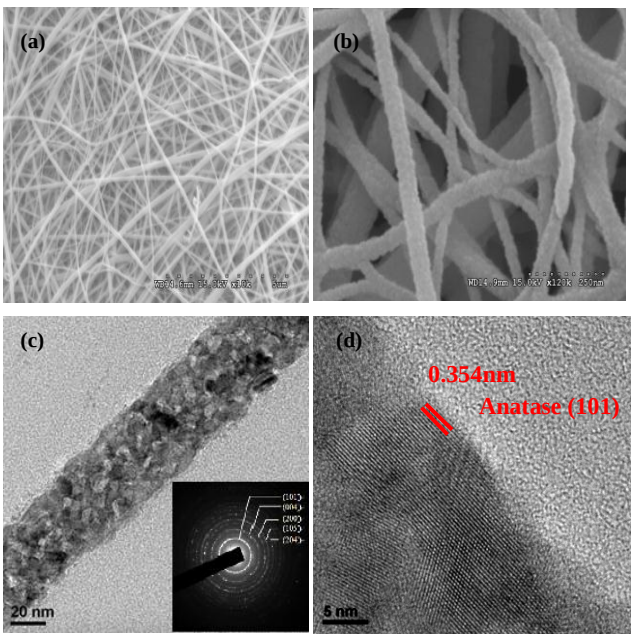

Fig 3. (a) SEM image of the regular TiO_2 nanofibers. (b) Magnified SEM image of the regular TiO_2 nanofibers. (c) TEM image of the regular TiO_2 nanofibers and corresponding SAED pattern. (d) HRTEM image of the anatase crystals indicated by red lines.

b. Texture property

Figure 4 (a) shows the N_2 adsorption-desorption isotherms of the hollow mesoporous TiO_2 nanofibers and regular TiO_2 nanofibers. All the fibers exhibit the type IV isotherm curves with well-defined characteristic condensation step at P/Po ~ 0.3–0.5. It clearly indicates that TiO_2 possessed mesoporous structure.[23,24] The point of inflection of P/Po ~ 0.4 (hollow mesoporous nanofibers) is characteristic of capillary condensation within the uniform mesopores.

The intersection point in N_2 adsorption and desorption curves of

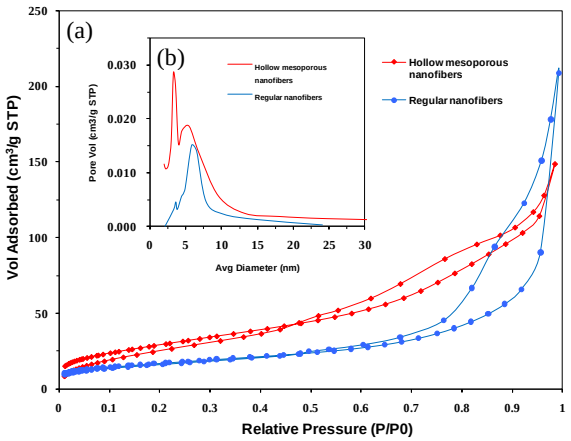

Fig 4. (a) N_2 adsorption and desorption isotherm of regular TiO_2 nanofibers and hollow mesoporous TiO_2 nanofibers. (b) Pore size distribution (inset) of regular TiO_2 nanofibers and hollow mesoporous TiO_2 nanofibers.

Table 1: Texture properties of Electrospun TiO_2 nanofibers

Morphology	BET Surface area (m^2/g)	Avg Pore diameter (nm)	Total Pore volume (cm^3/g)	Dimensions
Hollow Mesoporous Nanofibers	118	8.6	0.281	d =130 ± 80 nm d_w=28 ± 18 nm
Regular Nanofibers	59	11.3	0.168	d =100 ± 63 nm

d_w is the thickness of mesoporous wall.

hollow mesoporous TiO_2 nanofibers demonstrate that there were mainly two sizes of pores on the surface. The two types of mesopores; 3.2 nm and 5.4 nm in hollow mesoporous TiO_2 nanofibers were observed in the pore size distribution curve (Figure 4 (b)). This effect is ascribed to the evaporation of two polymers; PEO and PVP that were removed during sintering from core and shell components of the nanofibers respectively. These polymers have different thermal degradation temperature and different size and shape. The evaporation of the polymers from the solution will leave void space/pores inside the structure. The pore size distribution was calculated based on Barrett-Joyner-Halenda (BJH) method. Narrow pore-size distribution with pore diameter of 5.8 nm was observed for regular TiO_2 nanofibers. The Brunauer–Emmett–Teller (BET) surface area, average pore diameter and total pore volume are summarized in Table 1. BET study revealed that the hollow mesoporous TiO_2 nanofibers had surface area of 118 m^2/g, which is about 2 times higher than that of regular TiO_2 nanofibers (59 m^2/g). The average pore diameter further confirmed the mesoporous structure of hollow mesoporous TiO_2 nanofibers. The total pore volumes of hollow mesoporous TiO_2 nanofibers and regular TiO_2 nanofibers were found to be 0.281 and 0.168 cm^3/g respectively, indicating the hollow mesoporous structure improve the porosity of one dimension nanofibers.

The surface area of the commercial P25 (Degussa AG, Frankfurt, Germany) was measured to be 53 m^2/g and the comparison of P25 and hollow mesoporous TiO_2 nanofibers on the electrochemical properties and photocatalytic activities were also discussed in this report.

c. Photovoltaic performance

Photovoltaic properties of as-prepared TiO_2 architectures were evaluated by constructing DSSCs and the overall light-to electrical energy conversion efficiency was evaluated using the equation $\eta = FF \cdot Jsc \cdot Voc/P_{in}$, where FF is the fill factor, Jsc is the short circuit current density, V_{OC} is the open circuit voltage, and P_{in} is the incident light power density. Figure 5 shows the photocurrent density vs. voltage (J-V) characteristics of DSSCs based on the hollow mesoporous and regular TiO_2 nanofibers.

Fig 6 compares the absorption spectrum of the N719 dye anchored on hollow mesoporous TiO_2 nanofibers and regular TiO_2 nanofibers. It showed that hollow mesoporous TiO_2 nanofibers with high surface area (118 m^2/g) absorbed more dye

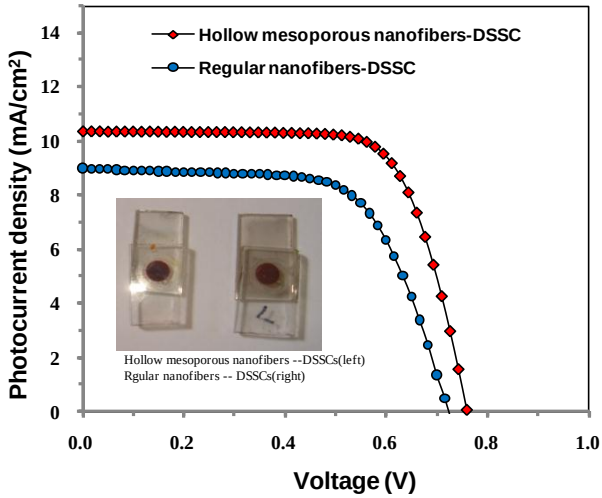

Fig 5. Photocurrent density-voltage curves of DSSC constructed with TiO_2 hollow mesoporous nanofibers and regular nanofibers photoanode. The inset is the photo of TiO_2 hollow mesoporous nanofibers based cell (left) and TiO_2 regular nanofibers based cell (right).

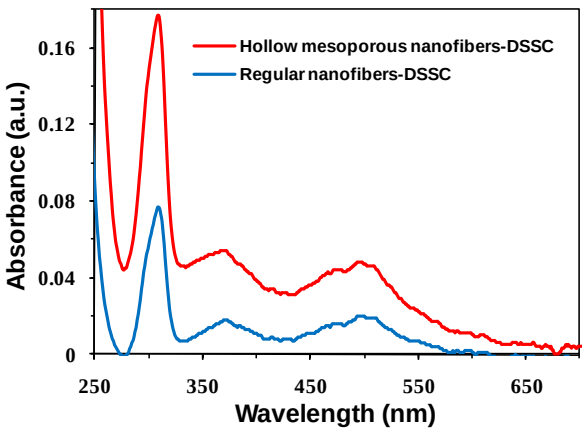

Fig 6. UV-vis absorption spectra of the absorbed dye molecules (N719 dye) on TiO_2 hollow mesoporous nanofibers and TiO_2 regular nanofibers based devices

than regular TiO_2 nanofibers (59 m^2/g). The amount of chemisorbed ruthenium dye (N719) was determined by Beer law,

$$A = \varepsilon C L \qquad (2)$$

where A is the light absorbance, ε is the molar absorptivity , L is the distance the light travels through the material and C is the concentration of absorbing dye molecules. The dye loading of hollow mesoporous TiO_2 nanofibers and regular TiO_2 nanofibers electrodes were calculated to be 3.86 and 1.68×10^{-6} mol/cm^2, respectively. This result revealed that the absorption intensity of dye molecules on the hollow mesoporous TiO_2 nanofibers electrode is 2 times more than that of regular TiO_2 nanofibers electrode of same thickness, indicating the enhancement of incident light absorption.

The calculated solar cell parameters were given in Table 2.

Table 2: Photovoltaic performance of DSSCs assembled by various morphologies of TiO_2

Morphology	J_{sc} (mA/cm^2)	V_{oc} (V)	FF	η (%)	Anchored dye (10^{-6} mol/cm^2)
Hollow mesoporous TiO_2 nanofibers based DSSC	10.38	0.758	0.72	5.61±0.06	3.86
Regular TiO_2 nanofibers based DSSC	8.99	0.738	0.64	4.17±0.08	1.68

The short circuit current (Jsc), open circuit voltage (Voc) and fill factor (FF) of the DSSC using the hollow mesoporous fibers were found to be 10.38 mA/cm^2, 0.758 V and 0.72 respectively.For regular TiO_2 nanofibers based DSSC, Jsc of 8.99 mA/cm^2, Voc of 0.738 and FF of 0.64, and power conversion efficiency of 4.17±0.08 % were obtained. The reduced current density obtained with regular TiO_2 nanofibers was due to insufficient light harvesting by TiO_2 films. Lower surface area of regular TiO_2 nanofibers limited the anchoring of more dye molecules on the surface of TiO_2 films, thus leading to poor optical absorbance. The conversion efficiency of DSSC using hollow mesoporous TiO_2 nanofibers was about 1.4 times higher than that of DSSC using regular TiO_2 nanofibers. The improved energy conversion efficiency was mainly from the increase in Jsc compared to that for regular nanofibers based DSSCs, indicating hollow mesoporous structure facilitates the electron injection density with large interface between dye molecules and nanofibers.

The higher surface area is related to the larger amount of adsorbed dyes. V_{OC} is related to the energy gap between Fermi level of semiconductor and Nernst potential of redox couple.[25] For the same film thickness, it is influenced by the electron affinity of semiconductor, ionization potential of dye and the dark current. Raising the conduction band of semiconductor can reduce the recombination loss, which results in higher open circuit voltage.[26] The V_{OC} was found to be improved for the hollow mesoporous TiO_2 nanofibers based DSSC, attributes to better penetration of electrolyte into TiO_2 electrode, which suppressed back electron transfer and enhanced the redox process between dye molecules and electrolyte. The presence of mesoporous structure promotes better contact with electrolyte and more adsorption of the dye in the hollow nanofibers. The retardation of surface recombination between conduction band electrons and I_3^- species in the Nernst potential of electrolyte in hollow mesoporous nanofibers should be able to offset the

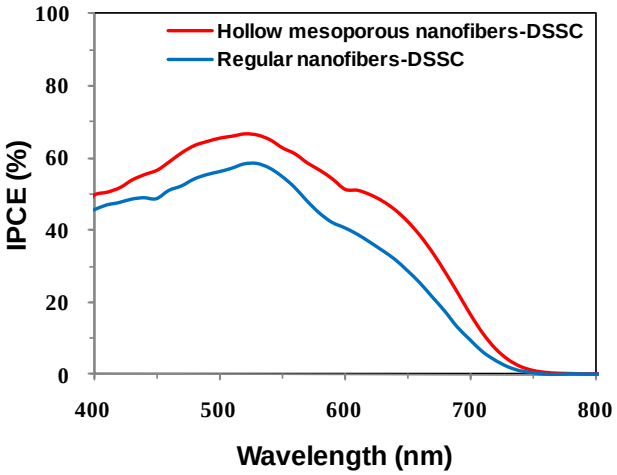

Fig 7. IPCE spectra of DSSC constructed with TiO_2 hollow mesoporous nanofibers and TiO_2 regular nanofibers based devices

adverse shift of the band edge toward positive potential and produce a net V_{OC} gain of about 20 mV. In literature, TiO_2 nanorods/nanofibers based DSSCs was reported to have the efficiency η up to 7.2 %, which was however achieved using the C101 dye.[27] C101 dye possesses heteroleptic polypyridyl ruthenium(II) complex structure, is characterized by a high molecular extinction coefficient that facilitated for conversion efficiency of 7.2 %. Efforts aiming at decreasing the diameter of nanofibers and thus increasing the roughness factor of fibrous photoelectrode are currently pursued by us.

Incident photo-to-current conversion efficiency (IPCE) of device fabricated by hollow mesoporous TiO_2 nanofibers and regular TiO_2 nanofibers are showed in Figure 7. The IPCE value was determined by IPCE (λ) = LHE (λ) φ_{inj} η_c, [28] where LHE (λ) is the light harvesting efficiency for photons of the wavelength λ, φ_{inj} is the quantum yield for electron injection and η_c is the electron collection efficiency. The maximum IPCE was increased from 58.6 % to 67 % at 520 nm by hollow mesoporous TiO_2 nanofibers based cells. The improvement of ~15% suggests that the devices based on hollow mesoporous TiO_2 nanofibers have more electrons injection and better electron transportation behaviour than that of regular TiO_2 nanofibers. Although the electron transportation obtained with the single-crystal electrode is theoretically higher than that obtained from polycrystalline form due to the lack of domain boundaries and defect in the single crystal, Gratzel et al. demonstrated that the IPCE value obtained with the single-crystal TiO_2 anatase electrode was much smaller than that of polycrystalline TiO_2 anatase electrode. This dramatic improvement is mainly due to the better light harvesting of the dye-sensitized polycrystalline.[7] A. J. Frank et al. further

proved that anatase film was 25% and 14% higher of rutile film in the overall energy conversion efficiencies and incident photon-to-current conversion efficiency respectively, which is mainly due to difference in their surface area (i.e the amount of dye adsorbed).[29] The 1-D hollow dimensional anatase film having high surface area synthesized by electron-spinning method could be one possible solution to the high efficiency electron conductor in the DSSCs.

d. Electronic transport analysis

To investigate the transport characteristic of injected electron in hollow mesoporous TiO_2 nanofibers film and the electron recombination between quasi Fermi level and redox potential, the electrochemical impedance spectroscope (EIS) technique was carried out. Figure 8 shows a general transmission line model which was developed by Bisquert et al.[30]. Various interfaces in DSSC were modeled by parallel RC circuit. Resistance element models charge exchange and constant phase element (CPE) denotes charge accumulation at double layer interface. The I_3^- redox process in electrolyte was modeled by a finite Warburg element. By fitting the impedance spectra, the electron recombination lifetime (τ_n) and collection lifetime (τ_d) were calculated using the correlation $\tau_n = (R_{ct}Q_k)^{1/\beta}$ and $\tau_d = (R_tQ_k)^{1/\beta}$,where β is the CPE exponent. The effective electron diffusion coefficient was measured as follows; $D_{eff} = L^2/\tau_d$.

Figures 9 (a) and (b) illustrate electron diffusion coefficient (D_{eff}) and recombination lifetime (τ_n) in transmission line model, compared to the data of regular TiO_2 nanofiber based DSSC from our previous research work [31] and P25 TiO_2 nanoparticles based

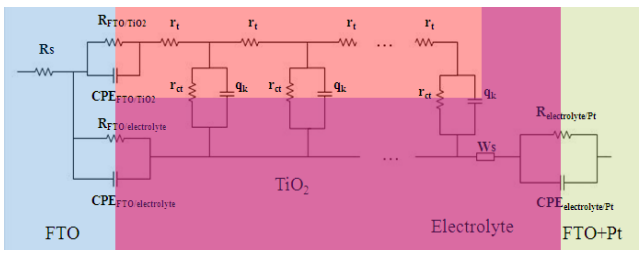

Fig 8. Transmission line model of DSSC. $R_{FTO/TiO2}$, $R_{FTO/electrolyte}$ and $R_{electrolyte/Pt}$ are the charge transfer resistance at the FTO-TiO_2 , FTO-electrolyte and electrolyte-Pt interfaces respectively; $CPE_{FTO/TiO2}$, $CPE_{FTO/electrolyte}$ and $CPE_{electrolyte/Pt}$ are the double layer capacitance between FTO-TiO_2 , FTO-electrolyte and electrolyte-Pt contacts respectively; r_t is the transport resistance of TiO_2 film, r_{ct} and q_k are the electron transfer resistance chemical capacitance contribute by the electronic states and the space charge of electron recombination process between TiO_2 film and I_3^- electrolyte; Rs is the series resistance including the sheet resistance of FTO glass and the contact resistance of the cell.

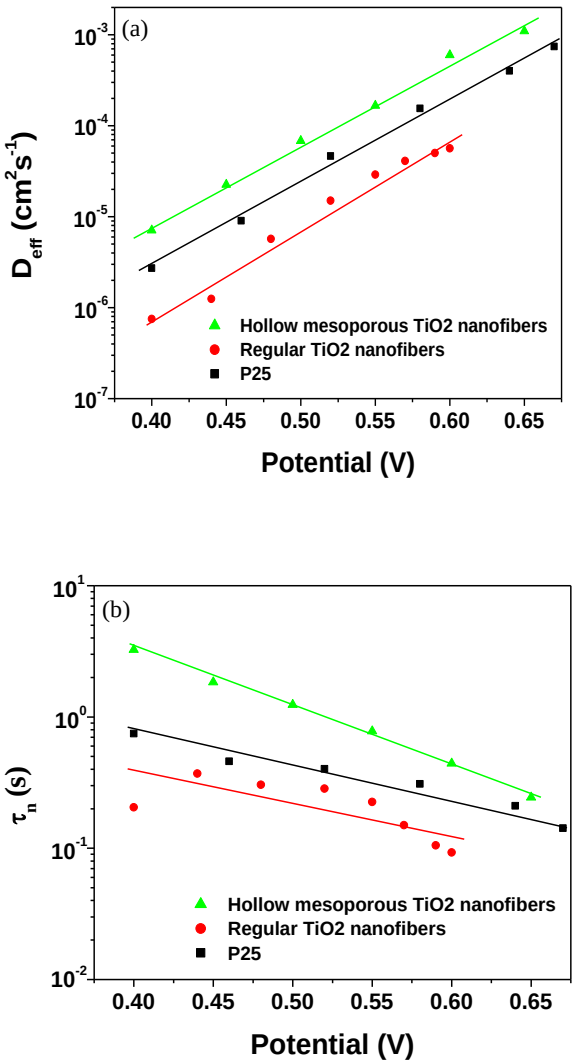

Fig 9. (a) Effective electron diffusion coefficient D_{eff}. (b) Electron recombination lifetime τ_n.

DSSC (Jsc = 10.07 mA/cm^2, Voc = 0.748 V, FF = 0.65, η = 5.02 ± 0.13 %). The fitting results of electron transport resistance R_t, electron recombination resistance R_{ct}, chemical capacitance Q_k are shown in the supporting information. The electron effective diffusion coefficient of hollow mesoporous TiO_2 nanofibers, P25 nanoparticles and regular TiO_2 nanofibers based DSSCs showed a decrease in the following order; hollow mesoporous TiO_2 nanofibers > P25 nanoparticles > regular TiO_2 nanofibers. It suggests that one dimensional (1D) hollow mesoporous TiO_2 nanofibers with closely packing of grains and crystals intergrowth with each other has better directivity. Higher surface area of the hollow mesoporous morphology allowed for anchoring of more dye molecules and better electrolyte penetration which resulted in

faster electron diffusion and shortened the electron collection time. In the electron recombination between Femi level and Nernst potential, the electron recombination resistance of hollow mesoporous TiO_2 nanofibers based DSSCs were found to be higher than that of P25 nanoparticles, and also regular TiO_2 nanofibers based DSSCs. The chemical capacitance of hollow mesoporous TiO_2 nanofibers was slightly lower than that of P25 nanoparticles, which reveals relatively lower charge accumulated in the space charge region of 1D nanostructure. The electron recombination life time was found to be decreased in the following order; hollow mesoporous TiO_2 nanofibers > P25 nanoparticles > regular TiO_2 nanofibers, indicating electron recombination rate is slower in hollow mesoporous TiO_2 nanofibers. It may be ascribed to the higher surface area of hollow mesoporous TiO_2 nanofibers that increase the effective contact point between TiO_2 grains and triiodide in electrolyte. Higher surface area of nanofibers showed a positive effect of electron trapping and de-trapping on the surface of nanofibers and suppresses the electron back reaction. Gratzel et al. demonstrated that the trapping of carrier reduced in TiO_2 fibers and electron transfer rate to the dye oxidized state was higher than that of the TiO_2 nanoparticulate. This accelerating effect is attributed to the particular morphology of pores surrounding the oxide fibers. Triiodide ions in the electrolyte have the possibility to escape faster and farer and to diffuse more freely to the counter electrode in the one dimensional (1D) nanofibers mat. [27] Although high surface area give rise to defect states in the bandgap that perform as trap centers for the free carriers, this slow down effect was overcome by the large promotional effect of 1D nanofiber structure.

e. Photocatalytic activities

The photocatalytic performance of hollow mesoporous TiO_2 nanofibers was evaluated by carrying out the degradation study on rhodamine B dye. Commercial P-25 (Degussa AG, Frankfurt, Germany) was also adopted for a comparison purpose. The photodegradation profiles (concentration change) of rhodamine B in the presence of hollow mesoporous TiO_2 nanofibers and P25 TiO_2 NPs under visible light irradiation are shown in Fig 10 (a). Rhodamine B was clearly seen stable in the absence of catalysts. The decomposition rate (C/C_0) of hollow mesoporous TiO_2 nanofibers was observed to be higher than that of P25. Using Langmuir-Hinshelwood model, the degradation profile of

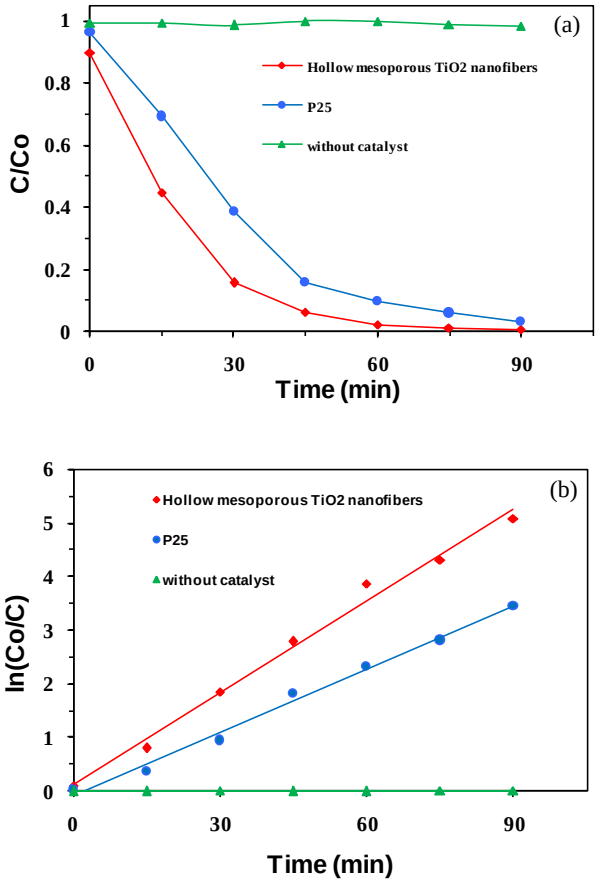

Fig 10. Photocatalytic degradation profile of rhodamine B (a) and kinetic linear simulation curve (b) over hollow mesoporous TiO_2 nanofibers and P-25.

Fig 10 (a) was converted to kinetic plot. Fig 10 (b) shows that the kinetic plots of hollow mesoporous TiO_2 nanofibers and P25 approximately followed first order. The apparent rate constant k_{app} was determined by

$$\ln(C_0/C) = k_{app}t \quad [32] \qquad (3)$$

The value of k_{app} was calculated to be 0.061 min^{-1} for hollow mesoporous TiO_2 nanofibers and 0.039 min^{-1} for P25. The enhanced photodegradation activity is attributed to the factors including surface area, grain size, crystalline and morphology.[33-37] As the catalytic activity takes place on the surface of the photocatalyst in general, major contributing factor is that higher surface area (118 m^2/g) of hollow porous TiO_2 fibers than that of P25 (53 m^2/g). Another possible factor can be ascribed to grain size (9.6 nm) of hollow mesoporous nanofibers, which is significantly smaller than that of P25 (20.3 nm). These factors might act as charge separation center for enhancing photoexcited electron-hole separation.

Conclusions

Electrospinning has so far been used for producing anatase 1D TiO_2 in either hollow form or mesoporous structure. Herein we demonstrated for the first time that the individual anatase TiO_2 fiber was possessed with both hollow and mesoporous structures by selecting suitable polymers, optimising the polymer/precursor ratio and post- process condition. Annealing of core-shell nanofibers prepared using PEO/TiO_2-PVP at 450°C for 1 h at a heating rate of 2°C /min yielded hollow mesoporous structure in TiO_2 nanofibers. The method presented in this study is the undoubtedly cost-effective approach in making high surface area TiO_2 nanofibers by electrospinning, and also potential alternative to the currently available methods like hydrothermal synthesis, conventional electrospinning and template assisted fabrication. Compare to regular TiO_2 nanofibers based DSSCs, the enhancement of power conversion efficiency was observed in hollow mesoporous nanostructured TiO_2 fibers, due to more dye loading and faster electron transport. The characteristics of transient photocurrent/photovoltage measurements on hollow mesoporous TiO_2 nanofibers are under further investigation. Hollow mesoporous TiO_2 nanofibers should offer obvious advantages that would inspire for new developments in the design of high efficient heterojunction structures in DSSCs and hybrid solar cells applications. The hollow mesoporous TiO_2 nanofibers also showed higher catalytic activity than that of TiO_2 nanoparticles, which is attributed to its higher surface area that enabled the strong interactions between the TiO_2 and dye. Studies of the catalytic mechanism of TiO_2 nanofibers on the various organic pollutants and relation between materials morphology and surface structure verses organic molecular structures are currently under investigation.

Acknowledgement

The authors gratefully acknowledge the financial support of the NTU-NUS (NRF-CRP-4-2008-03).

Notes and references

1.L. Li, X. Yin, S. Liu, Y. Wang, L. Chen and T. Wang, *Electrochem. Commun*, 2010, **12**, 1383-1386.
2.G. Lee, J.-C. Song and K.-B. Yoon, *Macromol. Res*, 2010, **18**, 571-576.
3. X. T. Dong, J. X. Wang, Q. Z. Cui, G. X. Liu and W. S. Yu, *Int. J. Chem*, 2009, **1**, 13-17.
4. M. Chen and F. Besenbacher, *ACS Nano*, 2011, **5**, 1549-1555.
5. B. O'Regan and M. Gratzel, *Nature*, 1991, **353**, 737-740.
6. M. K. Nazeeruddin, A. Kay, I. Rodicio, R. Humphry-Baker, E. Mueller, P. Liska, N. Vlachopoulos and M. Graetzel, *J. Am. Chem. Soc*, 1993, **115**, 6382-6390.
7. M. Gratzel, *Nature*, 2001, **414**, 338-344.
8. M. Grätzel, *Inorg.Chem*, 2005, **44**, 6841-6851.
9. S. Ito, P. Chen, P. Comte, M. K. Nazeeruddin, P. Liska, P. Péchy and M. Grätzel, *Prog. Photovoltaics*, 2007, **15**, 603-612.
10. F. Meng, X. Song and Z. Sun, *Vacc*, 2009, **83**, 1147-1151.
11. S. Uchida, R. Chiba, M. Tomiha, N. Masaki, M. Shirai, *Denki Kagaku oyobi Kogyo Butsuri Kagaku*. 2002, **70**, 418-420.
12. G. K. Mor, K. Shankar, M. Paulose, O. K. Varghese and C. A. Grimes, *Nano.Lett*, 2005, **6**, 215-218.
13. O. K. Varghese, M. Paulose and C. A. Grimes, *Nature Nano*, 2009, **4**, 592-597.
14. I. C. Flores, J. N. de Freitas, C. Longo, M.-A. De Paoli, H. Winnischofer and A. F. Nogueira, *J. Photochem. Photobio. A*, 2007, **189**, 153-160.
15. Z. Qi, H. Yu, Y. Chen and M. Zhu, *Mater. Lett*, 2009, **63**, 415-418.
16. D. Li and Y. Xia, *Nano Lett*, 2004, **4**, 933-938.
17. I.-D. Kim, A. Rothschild, B. H. Lee, D. Y. Kim, S. M. Jo and H. L. Tuller, *Nano Lett*, 2006, **6**, 2009-2013.
18. B. H. Lee, M. Y. Song, S.-Y. Jang, S. M. Jo, S.-Y. Kwak and D. Y. Kim, *J. Phys. Chem. C*, 2009, **113**, 21453-21457.
19. S. Pavasupree, S. Ngamsinlapasathian, M. Nakajima, Y. Suzuki and S. Yoshikawa, *J Photochem. Photobiol. A*, 2006, **184**, 163-169.
20. C. M. Lofton, C. B. Milz, H. Huang and W. M. Sigmund, *J. Eur. Ceram. Soc*, 2005, **25**, 883-889.
21. G. Taylor, *Proc. Roy. Soc. London. Ser. A*, 1964, **280**, 383-397.
22. A. L. Patterson, *Phys. Rev*, 1939, **56**, 978-982.
23. A. E. Ahmed and F. Adam, *Microporous Mesoporous Mater*, 2007, **103**, 284-295.
24. N. Hosseinpour, A. A. Khodadadi, Y. Mortazavi and A. Bazyari, *Appl. Catal. A*, 2009, **353**, 271-281.
25. S. E. Shaheen, C. J. Brabec, N. S. Sariciftci, F. Padinger, T. Fromherz and J. C. Hummelen, *Appl. Phys. Lett*, 2001, **78**, 841-843.
26. C.J. Brabec, A. Cravino, D. Meissner, N.S. Sariciftci, T. Fromherz, M.T. Rispens, L. Sanchez, J.C. Hummelen, *Adv. Funct. Mater*, 2001, **11**, 374–380.
27. E. Ghadiri, N. Taghavinia, S. M. Zakeeruddin, M. Grätzel and J.-E. Moser, *Nano Lett*, 2010, **10**, 1632-1638.
28. B. A. Gregg, *J. Phys. Chem. B*, 2003, **107**, 4688-4698.
29. N. G. Park, J. van de Lagemaat and A. J. Frank, *J.Phys.Chem.B*, 2000, **104**, 8989-8994.
30. J. Bisquert, G. Garcia-Belmonte, F. Fabregat-Santiago and A. Compte, *Electrochem. Commun*, 1999, **1**, 429-435.
31. K. Mukherjee, T.-H. Teng, R. Jose and S. Ramakrishna, *Appl. Phys. Lett*, 2009, **95**, 012101.
32. A. K. L. Sajjad, S. Shamaila, B. Tian, F. Chen and J. Zhang, *J. Hazard. Mater*, 2010, **177**, 781-791.
33. K.L. Zhang, C.M. Liu, F.Q. Huang, C. Zheng, W.D. Wang, *Appl. Catal. B*. 2006, **68**, 125-129.
34. J.C. Yu, J.G. Yu, W.K. Ho, L.Z. Zhang, *Chem.Commun*. 2001, **3**, 1942-1943.
35. T. Park, S.A. Haque, R.J. Potter, A.B. Holmes,J.R. Durrant, *Chem. Commun*. 2003, **13**, 2878-2879.
36. Z. Liu, D. D. Sun, P. Guo and J. O. Leckie, *Nano Lett*, 2006, **7**, 1081-1085.
37. D. Li and Y. Xia, *Adv. Mater*, 2004, **16**, 1151-1170.